EASR

Engineering and Applied Science Research

https://www.tci-thaijo.org/index.php/easr/index

Published by the Faculty of Engineering, Khon Kaen University, Thailand

Optimization of green-synthesized silver nanoparticles using *Mimosa pudica* L. for enhanced photocatalytic degradation of methylene blue: A response surface methodology approach

Pharini Chaison[1)], Wimonrat Tongpoothorn[2)], Kitiyaporn Wittayanarakul[3)] and Manop Sriuttha*[3)]

[1)]Program in Applied Bioresource Science, Faculty of Interdisciplinary Studies, Khon Kaen University, Nong Khai Campus, Nong Khai 43000, Thailand
[2)]Department of Chemistry, Faculty of Engineering, Rajamangala University of Technology Isan, Khon Kaen Campus, Khon Kaen 40000, Thailand
[3)]Program in Science Technology and Business Enterprise, Faculty of Interdisciplinary Studies, Khon Kaen University, Nong Khai Campus, Nong Khai 43000, Thailand

Received 15 September 2024
Revised 31 January 2025
Accepted 6 February 2025

Abstract

Silver nanoparticles (AgNPs) were synthesized using *Mimosa pudica* L. leaf extract as a reducing and stabilizing agent. AgNP yield was maximized using central composite design (CCD) based on response surface methodology (RSM). An $AgNO_3$ concentration of 3.06 mM, 732 µL extract volume, a 616 W microwave power level, and a 2.35 min reaction time were optimal conditions. Extract volume showed the highest impact on synthesis (F-value: 795.57), followed by microwave power (F-value: 168.84), reaction time (F-value: 51.38), and $AgNO_3$ concentration (F-value: 49.72). UV-Vis spectrophotometry (UV-Vis) was used to characterize the synthesized AgNPs. A surface plasmon resonance (SPR) peak at 428 nm was observed. It was found from diffuse reflectance spectroscopy (DRS) that the bandgap is 2.34 eV. Fourier transform infrared spectroscopy (FTIR) confirmed the presence of functional groups of plant metabolites that served as capping and reducing agents. Spherical nanoparticles with an average diameter of 7.39±2.37 nm were observed under transmission electron microscopy (TEM). XRD analysis confirmed the face-centered cubic crystalline structure of AgNPs. EDX was employed to study the elemental composition. Synthesized AgNPs were assessed as a photocatalyst for methylene blue degradation under solar light irradiation. A 79.07% conversion was achieved under optimized conditions. Kinetic studies revealed that the degradation of methylene blue followed a pseudo-second-order model with a rate constant of 0.0929 mg^{-1} L min^{-1} and R^2 of 0.9990. This green synthesis is a viable, sustainable, and cost-effective way to prepare AgNPs with good photocatalytic properties.

Keywords: Silver nanoparticles, Methylene blue, Response surface methodology, Photocatalytic degradation, *Mimosa pudica* L.

1. Introduction

Water pollution is a serious global environmental problem caused by emissions of industrial effluents containing synthetic dyes and dangerous chemicals such as heavy metals, pesticides, and fertilizers [1, 2]. The complex aromatic molecular structures of these pollutants make them stable in the environment and they are poorly biodegradable [3-6]. Methylene blue (MB), is a common cationic dye used in textiles, chemical indicators, and the pharmaceutical industry. It can badly damage the environment even at low concentrations through its capability to decrease light penetration and reduce dissolved oxygen levels, thereby greatly harming aquatic ecosystems [7-9].

Numerous treatment processes have been designed to mitigate dye pollution through adsorption, chemical oxidation, catalytic reduction, and photocatalysis [10, 11]. Recent advances in nanotechnology have enabled development of environmentally friendly solutions through the synthesis of noble metal nanoparticles with precisely controlled shapes and sizes [12, 13]. Of these, silver nanoparticles (AgNPs) have attracted special attention because of their high photocatalytic activity, surface plasmon resonance properties, and their capability to generate reactive oxygen species upon illumination [14, 15]. Use of AgNP-containing membranes span diverse industries such as food processing, cosmetics, textile manufacturing, and catalytic reactions [16].

However, conventional chemical synthesis involves great risk to the environment, while green synthesis using plant extracts is a more environmentally friendly approach [17, 18]. *Mimosa pudica* L. can be used in these types of solutions [19]. Various bioactive compounds such as alkaloids, phenols, flavonoids, tannins, and terpenoids [20-22] present in the plant can effectively reduce metal ions and stabilize nanoparticles [23, 24].

Synthesis of AgNPs and dye degradation involves many parameters such as concentration of reactants, pH, temperature, and reaction time [25]. Understanding the complex interaction amongst all these factors in the real world is infeasible with traditional one-factor-at-a-time optimization approaches [26]. Response surface methodology (RSM) is a powerful statistical tool for simultaneously optimizing multiple variables in both synthesis and degradation processes [27, 28].

*Corresponding author.
Email address: manosr@kku.ac.th
doi: 10.14456/easr.2025.14

In particular, using *Mimosa pudica* L. extract for synthesis of AgNPs and optimization of both synthesis and photocatalytic activity has not been comprehensively reported. In this work, a model and optimization of the green synthesis of AgNPs and the subsequent photodegradation of MB under solar light using RSM are first reported in the current study. Characteristics of the synthesized AgNPs were investigated using UV visible spectrophotometry (UV-Vis), diffuse reflectance spectroscopy (DRS), transmission electron microscopy (TEM), Fourier transform infrared spectroscopy (FTIR), X-ray diffraction (XRD) and energy dispersive X-ray spectroscopy (EDX) analyses. The photocatalytic efficiency of the synthesized AgNPs was determined from the degradation of MB at an optimized dye concentration, catalyst volume, and reaction time under natural sunlight conditions. This was done to determine the efficiency of the synthesized AgNPs in degrading MB.

2. Materials and methods

2.1 Materials and chemicals

Silver nitrate ($AgNO_3$) was purchased from Fisher Chemical, UK. Methylene blue ($C_{16}H_{18}ClN_3S$) was obtained from Quality Reagent Chemical, New Zealand. *Mimosa pudica* L. leaves were collected around Khon Kaen University, Nong Khai Campus, Thailand. All solutions were prepared with deionized water (DI).

2.2 Preparation of Mimosa pudica L. leaf extract

Mimosa pudica L. leaves were washed with tap water to remove contaminants. The leaves were dried at room temperature under ambient and shaded conditions. Fine powders (<2 mm) were obtained from the mechanically ground and sieved material (room temperature and shade dried) passing a No. 10 sieve. These powders were stored in a plastic bag at ambient temperature. 10 grams of powder was mixed with 200 mL of DI water. After that, the mixture was heated in a microwave oven at 300 W for 2 min. Then, it was filtered through Whatman No.1 filter paper. The filtrate solution was allowed to cool to room temperature. It was then stored at 4 °C for further analysis.

2.3 Green synthesis and optimization of AgNPs using Mimosa pudica L. by RSM

AgNPs were synthesized using $AgNO_3$ as a precursor with *Mimosa pudica* L. leaf extract as a reducing agent. Four parameters, $AgNO_3$ concentration (A), the volume of the plant extract (B), microwave power (C), and time (D) were examined as controlling factors. A range of leaf extract volumes (100-1000 µL) was mixed with 10 mL of $AgNO_3$ (1-5 mM). The mixtures were then microwave-heated at various power levels (100-800 W) for varying times (1-3 min). The solutions were made up to 50 mL with DI water in a volumetric flask after standing at room temperature for 1 hour. UV-Vis spectroscopy was done over the 300-800 nm range and confirmed the formation of AgNPs, as the solution color changed from light yellow to brownish red. Experimental values, as well as coded variables and study levels, are presented in Table 1. The second-order polynomial employed is shown as Equation 1. The optimized process was done using Design-Expert Version 13 (trial version) software for CCD with 30 runs (Table 2).

$$Y = \beta_0 + \beta_1 A + \beta_2 B + \beta_3 C + \beta_4 D + \beta_{12} AB + \beta_{13} AC + \beta_{14} AD + \beta_{23} BC + \beta_{24} BD + \beta_{34} CD + \beta_{11} A^2 + \beta_{22} B^2 + \beta_{33} C^2 + \beta_{44} D^2 \quad (1)$$

where Y is the predicted response, and β_0 is the regression coefficient. β_1, β_2, β_3, and β_4 are linear coefficients. β_{12}, β_{13}, β_{14}, β_{23}, β_{24}, and β_{34} are interaction coefficients. β_{11}, β_{22}, β_{33}, and β_{44} are quadratic coefficients. A, B, C, and D represent $AgNO_3$ concentration, extract volume, microwave power, and reaction time, respectively.

An F-test and correlation coefficient (R^2) were employed to assess the statistical significance and reliability of the fitted model. The model predictions were validated by comparing observed and predicted values of the synthesized AgNPs [26, 27, 29].

2.4 Characterization of optimized AgNPs using Mimosa pudica L.

Absorbance measurements were made using a UV-Visible spectrophotometer (Model UV-1900i, Shimadzu, Japan). A Tauc plot [30] was employed to estimate the band energy of AgNPs using the DRS spectra. Identification of the functional groups of AgNPs was done using a TENSOR 27 FTIR spectrometer (Bruker, USA). Characterization of the synthesized AgNPs examined their chemical composition, particle dimensions, and external surface using transmission electron microscopy (TEM) and energy dispersive spectroscopy (EDX) (TECNAI G2 20; FEI, USA). The crystallography of AgNPs was determined with an EMPYREAN X-ray diffractometer (Bruker USA).

Table 1 Independent variables, factors, and coded levels for the synthesis of AgNPs

Independent variable	Factors	Coded levels				
		-α	**-1**	**0**	**1**	**+α**
$AgNO_3$ concentration (mM)	A	1	2	3	4	5
Extract volume (µL)	B	100	325	550	775	1000
Microwave power (W)	C	100	275	450	625	800
Reaction time (min)	D	1.0	1.5	2.0	2.5	3.0

Table 2 Central composite design with RSM for synthesis of AgNPs

	Variables in coded levels				Synthesis of AgNPs	
Run	**A**	**B**	**C**	**D**	**Predicted**	**Actual**
1	4	775	625	1.5	1.584	1.589
2	3	550	800	2.0	1.423	1.376
3	4	775	275	1.5	1.363	1.338
4	2	775	625	1.5	1.462	1.498
5	2	325	625	2.5	0.984	1.020
6	3	550	450	2.0	1.230	1.307
7	3	550	450	3.0	1.368	1.388
8	4	775	275	2.5	1.551	1.488
9	3	550	450	2.0	1.371	1.307
10	3	100	450	2.0	0.435	0.419
11	3	550	100	2.0	0.773	0.829
12	2	325	625	1.5	0.828	0.869
13	4	325	625	2.5	1.056	1.067
14	3	1000	450	2.0	1.580	1.606
15	2	775	625	2.5	1.580	1.543
16	3	550	450	2.0	1.339	1.307
17	3	550	450	2.0	1.311	1.307
18	3	550	450	2.0	1.250	1.307
19	2	325	275	1.5	0.437	0.432
20	5	550	450	2.0	1.277	1.317
21	4	775	625	2.5	1.580	1.597
22	4	325	275	2.5	0.956	0.931
23	2	775	275	1.5	1.119	1.088
24	4	325	625	1.5	0.977	0.952
25	3	550	450	2.0	1.339	1.307
26	1	550	450	2.0	1.051	1.020
27	3	550	450	1.0	1.097	1.087
28	2	325	275	2.5	0.751	0.725
29	4	325	275	1.5	0.659	0.674
30	2	775	275	2.5	1.238	1.274

2.5 Photocatalytic decolorization of MB dye

The photocatalytic activity of the synthesized AgNPs was measured by comparing the absorbance of MB dye under solar light before and after its degradation. MB dye degradation was assessed by optimizing three parameters, reaction time (60-300 min), catalyst volume (1-10 mL), and dye concentration (2-10 mgL^{-1}). Different volumes of AgNP catalysts were combined with varying concentrations of MB (20 mL). The final volume of the mixture solutions was made up to 30 mL with DI water [31]. Investigations were conducted at a pH of 5.6, which is the normal acidity for dissolution of the desired molecules in DI water [32]. The mixtures were shaken at 150 rpm in the dark for 30 min to obtain adsorption/desorption equilibria [33]. These reactions were conducted from 11:00 AM to 1:00 PM for various time intervals [34]. The percent degradation was determined by measuring the absorbance of an aliquot (6 mL) of each run that was centrifuged at 9000 rpm for 5 min [35]. UV-Vis absorbance at 664 nm was employed to determine the MB concentration. The degradation performance of the catalysts was assessed following Eq. (2).

$$dye\ degradation\ (\%) = \frac{C_0 - C}{C_0} \times 100 \quad (2)$$

MB dye concentrations at the initial and final times are represented by C_0 and C, respectively [36]. This process degradation efficiency is highly sensitive to several operating parameters. Three parameters were selected for their effect on MB dye degradation, dye concentration (A), catalyst volume (B), and reaction time (C). These parameters were considered independent variables and were assessed using experimental design and statistical analysis [32] through their impact on the response function (*Y*, defined as the percent of MB degradation). The coded variables, experimental values, and levels are presented in Table 3. This experiment optimized a process through 20 runs (Table 4). Equation 3 shows a second-order polynomial that models MB degradation.

$$Y = \beta_0 + \beta_1 A + \beta_2 B + \beta_3 C + \beta_{12} AB + \beta_{13} AC + \beta_{23} BC + \beta_{11} A^2 + \beta_{22} B^2 + \beta_{33} C^2 \quad (3)$$

Y is the response function. β_0 is the regression coefficient and β_1, β_2, and β_3 are the linear coefficients. Interaction and quadratic coefficients are denoted by β_{12}, β_{13}, and β_{23}, as well as β_{11}, β_{22}, and β_{33}, respectively. The effects of the experimental variables on the response, both individually and in combination, are presented as 3D surface plots of the response and Equation 3. The quality and significance of the fitted model were determined using the F-test and the R^2 correlation coefficient. The model prediction was validated by comparison between the observed and predicted values of the photocatalytic degradation of MB dye [26, 27, 29].

Table 3 Experimental values and levels of independent variables for degradation of MB dye

Independent variable	**Factors**	**Coded levels**				
		-α	**-1**	**0**	**1**	**+α**
Dye concentration (mgL^{-1})	A	2.00	3.62	6.00	8.38	10.00
Catalyst volume (mL)	B	1.00	2.82	5.50	8.18	10.00
Reaction time (min)	C	60.00	108.65	180.00	251.35	300.00

Table 4 Runs of the experiment on CCD for the photocatalytic degradation of MB dye

Run	Independent variable			MB degradation (%)	
	A	B	C	Predicted	Actual
1	6.00	5.50	180.00	65.33	64.22
2	3.62	2.82	251.35	75.15	74.29
3	6.00	5.50	180.00	65.33	63.66
4	6.00	5.50	60.00	49.51	52.00
5	10.00	5.50	180.00	55.89	54.03
6	6.00	5.50	180.00	65.33	66.17
7	6.00	5.50	180.00	65.33	67.29
8	8.38	8.18	251.35	68.48	71.34
9	3.62	8.18	108.65	73.13	72.33
10	8.38	2.82	251.35	72.72	72.74
11	8.38	2.82	108.65	46.37	45.90
12	6.00	5.50	300.00	74.65	73.26
13	2.00	5.50	180.00	72.74	75.70
14	8.38	8.18	108.65	55.53	55.61
15	3.62	2.82	108.65	58.21	54.57
16	3.62	8.18	251.35	76.69	76.38
17	6.00	10.00	180.00	75.38	73.91
18	6.00	5.50	180.00	65.33	64.12
19	6.00	5.50	180.00	65.33	66.36
20	6.00	1.00	180.00	66.39	68.97

2.6 Kinetics study

Kinetic studies were performed under the optimum conditions for the photodegradation of MB dye using a catalyst volume of 8.20 mL and 3.64 mgL^{-1} of MB dye at different times (at pH 5.6). The solutions were agitated at 150 rpm in the dark for 30 min to reach an adsorption/desorption equilibrium. The reactions were done in daylight from 11:00 AM to 1:00 PM [34]. Experimental solutions were centrifuged at 9,000 rpm for 5 min [35]. The dye concentration change was determined by measuring MB dye absorbance at 664 nm under UV-Vis. Dye degradation kinetics were studied using pseudo-first-order and pseudo-second-order models.

2.7 Data analysis

Experimental designs and statistical analysis of the data were conducted using Design-Expert Version 13 (trial version). All experiments were performed with three replicates. The impacts of the different variables on the synthesis of AgNPs and photodegradation of MB were analyzed. 3D surface plots were developed. Analysis of variance (ANOVA) showed the significance of the variables. A regression model was developed and a coefficient of determination (R^2) presented. The fit quality and F-test were used to determine the statistical significance of the regression model.

3. Results and discussion

3.1 Green synthesis and optimization of AgNPs using Mimosa pudica L. *by RSM*

3.1.1 Statistical analysis for optimization of green synthesized AgNPs

ANOVA was performed to determine the correlation between the independent and response variables. The provided results include a Coefficient of Variation (C.V.), standard deviation (Std. Dev.), lack-of-fit, adequate precision, p-value, and F-value. Table 2 displays the CCD-based experimental results for green synthesis of AgNPs. Equation (4), which utilizes a second-order polynomial, shows the relationship between the parameters and the response to produce AgNPs. The predicted absorbance value for the synthesis of AgNPs is denoted by *Y*. This equation is most significantly influenced by the following order of equation coefficients: B (extract volume) > C (microwave power) > D (reaction time) > A ($AgNO_3$ concentration). The positive signs of these parameters indicate increased absorbance values for AgNP synthesis [29, 37].

$$Y = 1.31 + 0.0741A + 0.2965B + 0.1366C + 0.0754D + 0.0020AB - 0.0400AC - 0.0090AD - 0.0067BC - 0.0267BD - 0.0355CD - 0.0344A^2 - 0.0735B^2 - 0.0510C^2 - 0.0173D^2 \quad (4)$$

The models have excellent repeatability with low p-values and high F-values in Table 5. A model F-value of 83.20 for the synthesis of AgNPs indicates significance. All model terms are significant at $p<0.0001$. A C.V. value less than 10, indicates repeatability. In these experiments, the C.V. is 4.42, so the model is repeatable [38]. The lack-of-fit p-value is 0.6424, which is insignificant. Adequate precision (or signal-to-noise ratio) shows a value greater than 4 is preferable. This model has sufficient signal [29]. A suggested model for AgNP production using *Mimosa pudica* L. leaf extracts was developed using the experimental results, with values of R^2 and predicted R^2 within acceptable limits. R^2 (0.9873), adjusted R^2 (0.9754), and predicted R^2 (0.9479) indicate the model fit experimental data. There is good agreement between predicted and experimental values. ANOVA also showed a significant F-value and a p-value. Lack-of-fit was insignificant, with a high R^2 and low C.V. These statistics indicate the high validity of the model in predicting the quantity of AgNPs. The high R^2, adjusted R^2, and predicted R^2 values indicate a good fit between experimental and predicted data.

Table 5 Analysis of variance (ANOVA) for the synthesis of AgNPs

Source	SS	df	MS	F-Value	p-Value	Remark
Model	3.090	14	0.221	83.20	< 0.0001	Significant
A	0.132	1	0.132	49.72	< 0.0001	
B	2.110	1	2.110	795.57	< 0.0001	
C	0.448	1	0.448	168.84	< 0.0001	
D	0.136	1	0.136	51.38	< 0.0001	
AB	0.000	1	0.000	0.02	0.8813	
AC	0.026	1	0.026	9.64	0.0073	
AD	0.001	1	0.001	0.49	0.4932	
BC	0.001	1	0.001	0.27	0.6127	
BD	0.011	1	0.011	4.29	0.0561	
CD	0.020	1	0.020	7.62	0.0146	
A^2	0.033	1	0.033	12.27	0.0032	
B^2	0.148	1	0.148	55.87	< 0.0001	
C^2	0.071	1	0.071	26.89	0.0001	
D^2	0.008	1	0.008	3.08	0.0995	
Residual	0.040	15	0.003			
Lack of Fit	0.025	10	0.002	0.80	0.6424	Not significant
Pure Error	0.015	5	0.003			
Cor Total	3.130	29				

SS: sum of squares; df: degrees of freedom; MS: mean square; F: frequency; p: probability; R^2, 0.9873; Pred. R^2, 0.9479; Adj. R^2, 0.9754; Adequate Precision, 32.5693; C.V., 4.42%.

The coefficients suggest that these parameters positively affect the green synthesis of AgNPs. In Table 5, based on their p-values, the terms A, B, C, D, AC, CB, A^2, B^2, and C^2 are significant. The terms, AB, AD, BC, BD, and D^2, are insignificant. The corresponding F-values indicated that the extract volume (B) had the greatest impact, followed by microwave power (C), reaction time (D), and $AgNO_3$ concentration (A). Figure 1 displays a plot of the predicted versus actual response values. The high R^2 value, 0.9873, shows that the actual and predicted values are very close [27].

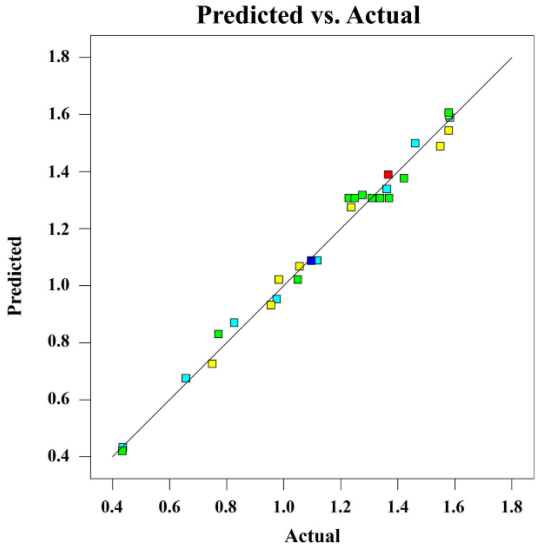

Figure 1 Predicted vs. actual values for synthesis of AgNPs using *Mimosa pudica* L. leaf extract

3.1.2 Interaction of parameters for the synthesis of AgNPs

3D response surface plots show the relationships between factors and their effects on the response surface. The designs for the response surface analysis of the absorbance values of AgNP production are shown in Figure 2.

Figure 2(a) shows that the synthesis of AgNPs increases with greater $AgNO_3$ concentrations and extract volumes. The relationship between $AgNO_3$ concentration and microwave power is depicted in Figure 2(b), showing a positive correlation between increased $AgNO_3$ concentration and microwave power, which results in enhanced synthesis of AgNPs. Figure 2(c) illustrates the relationship between $AgNO_3$ concentration and reaction time, showing a positive correlation between these two factors, indicating enhanced synthesis. Figure 2(d) shows the relationship between microwave power and extract volume. The synthesis of AgNPs increases with higher microwave power and greater extract volume. Figure 2(e) presents the relationship between extract volume and reaction time, indicating a positive correlation between increased extract volume and reaction time, resulting in enhanced synthesis of AgNPs. Figure 2(f) shows the relationship between microwave power and reaction time, suggesting a positive correlation between increased microwave power and longer reaction time, resulting in improved synthesis of AgNPs.

The concentration of $AgNO_3$, extract volume, microwave power, and reaction time have significant effects on the synthesis of AgNPs. This is also demonstrated in experiments using aloe vera extract [39]. The absorbance intensity with the $AgNO_3$ concentration, showed nanoparticle growth [33]. The absorbance value can be elevated by increasing the volume of plant extract [34, 35].

Biomolecules act as reducing agents and coat nanoparticle surfaces when a larger extract volume is used, preventing aggregation and enhancing their stability [40]. Increased microwave power corresponds to more input energy, which enhances the rate at which silver ions are reduced to AgNPs [41]. The intensity of the absorption increases with time [42]. A good SPR band was observed as the reaction time increased because a significant amount of Ag^{+} ions was transformed to Ag^{0} [18].

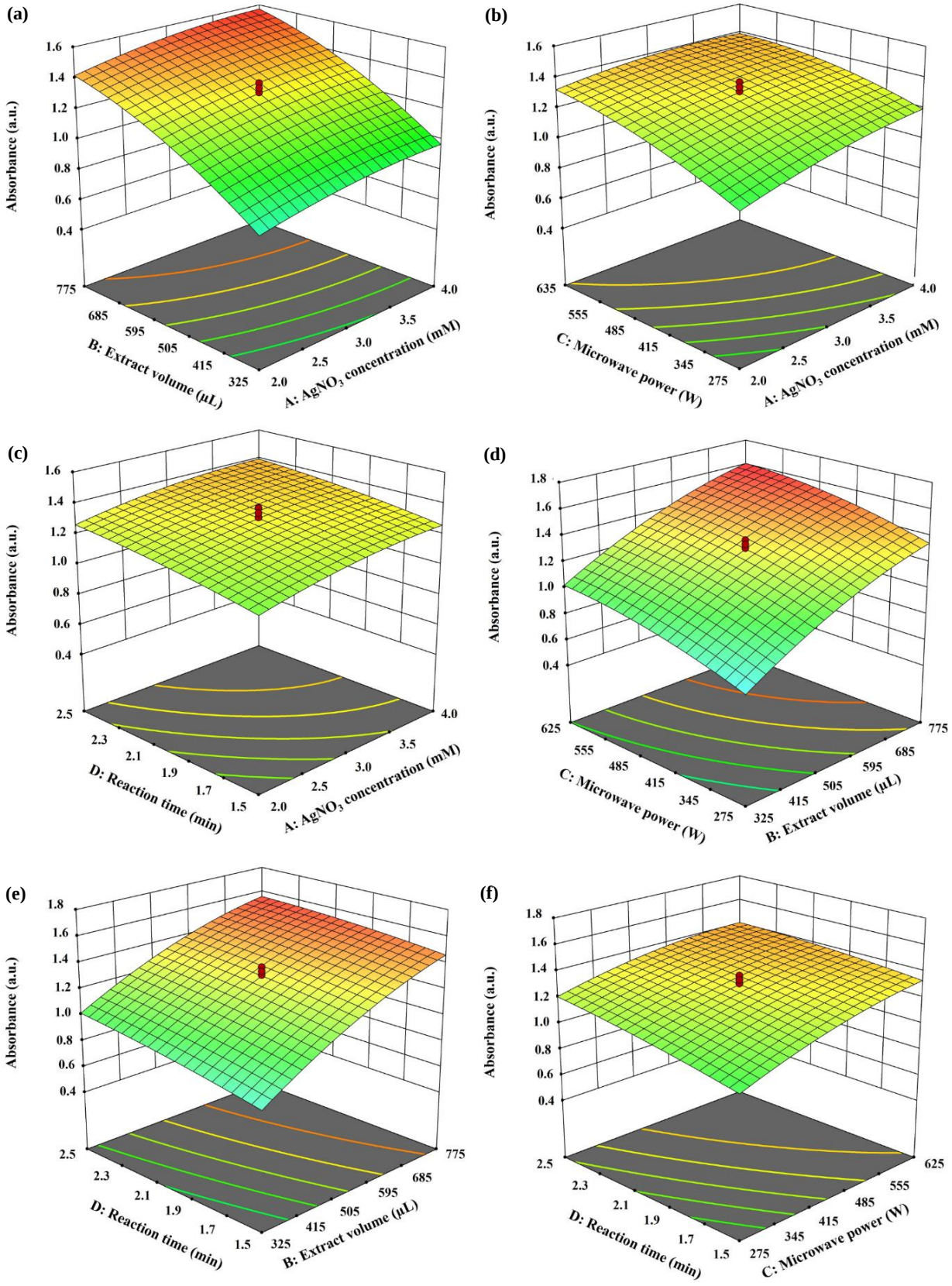

Figure 2 3D response surface plot of the effect of $AgNO_3$ concentration and extract volume (a), $AgNO_3$ concentration and microwave power (b), $AgNO_3$ concentration and reaction time (c), extract volume and microwave power (d), extract volume and reaction time (e), and microwave power and reaction time (f) for synthesis of AgNPs

3.1.3 Model validation

Experiments at the optimal conditions were run in triplicate to verify the precision and reliability of the applied CCD of the RSM, yielding a desirability value of 1.000 [43]. This reflects that the experimental conditions and model are favorable. Optimal values for the $AgNO_3$ concentration, extract volume, microwave power, and reaction time were 3.06 mM, 732 µL, 616 W, and 2.35 min, respectively. The optimized ramps are displayed in Figure 3. Under optimal conditions, the observed and expected values of AgNP absorbance at 664 nm were 1.558 and 1.584, respectively. The predicted and actual values were similar. This suggests that the applied model is correct and can be a useful tool to optimize AgNP synthesis [27, 29].

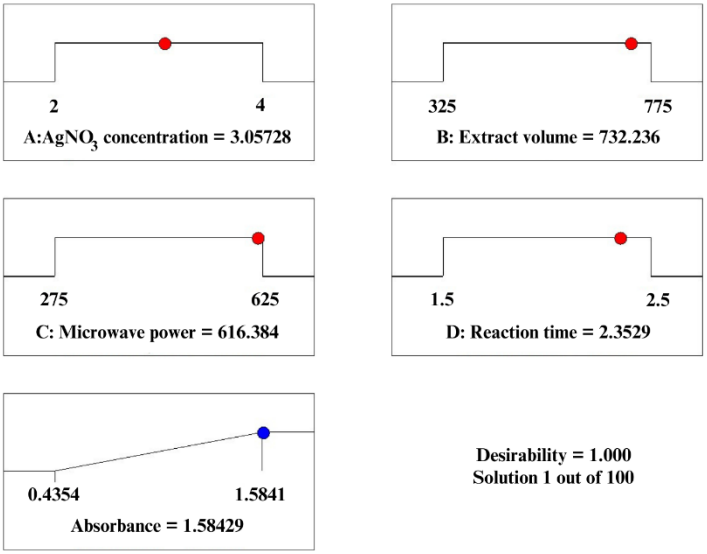

Figure 3 Optimized ramps for the synthesized AgNPs using RSM based on CCD

3.1.4 Proposed mechanism of AgNP formation using Mimosa pudica L. leaf extract

A proposed mechanism for synthesizing AgNPs using *Mimosa pudica* L. leaf extract is shown in Figure 4. The extract is rich in phytochemicals like flavonoids, polyphenols, tannins, and alkaloids [44]. Mimosine concentration was found using reverse-phase HPTLC [20]. Leaf extract alkaloids are reduced with silver ions (Ag^+) through hydroxyl (-OH) groups. Mimosine functions as a reducing and stabilizing scaffold for converting Ag^+ to Ag^0. This bioreduction [14] relies on the tautomeric transformation from an enol to keto form. During activation (Ag^+ reduction), nucleation and growth steps lead to the formation of particular-sized AgNPs. Finally, plant metabolites function as surface-capping agents, protecting the nanoparticles from agglomeration [18].

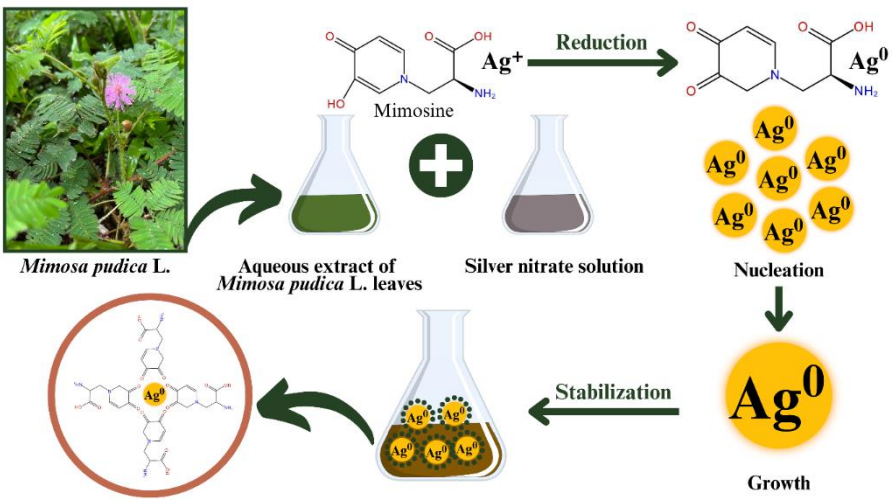

Figure 4 Proposed mechanism of AgNP formation using *Mimosa pudica* L. leaf extract

3.2 AgNP Characterization

3.2.1 UV-Vis and DRS analysis

UV-Vis can be used to confirm that metal nanoparticles have formed in aqueous solutions. The type of transition is electronic, from the valence to conduction bands. AgNP dispersions have strong colors owing to plasmon resonance absorption. Electron vibration modes are dependent on particle size and shape. They are responsible for characteristic absorption spectra in the UV-Vis region [45]. UV-Vis (300-800 nm) was used to monitor AgNP production. When an $AgNO_3$ solution was mixed with *Mimosa pudica* L. leaf extract,

and the resulting solutions were microwave heated, their color changed from yellow to brownish (Figure 5(a)). Synthesized AgNPs display a peak at 428 nm due to the formation of silver crystals, while neither $AgNO_3$ nor leaf extract had any peaks in the visible range. Ag^+ was reduced to Ag^0 by biomolecules in leaf extract and capped AgNPs [46].

Light absorption and its features were employed in the DRS technique to characterize AgNPs. The absorption edge for AgNPs was around 428 nm with a bandgap of about 2.34 eV (Figure 5(b)). This indicated that synthesized AgNPs were capable of absorbing visible light. Researchers derived sensitive AgNPs with green synthesis under visible light and used them for photocatalytic degradation [47]. Their low bandgap led to efficiently generating electron-hole pairs under visible light irradiation, resulting in high photocatalytic performance [47]. The bandgap energies of AgNPs from *Mimosa pudica* L. were comparable to those of *Plantago lanceolata* [48].

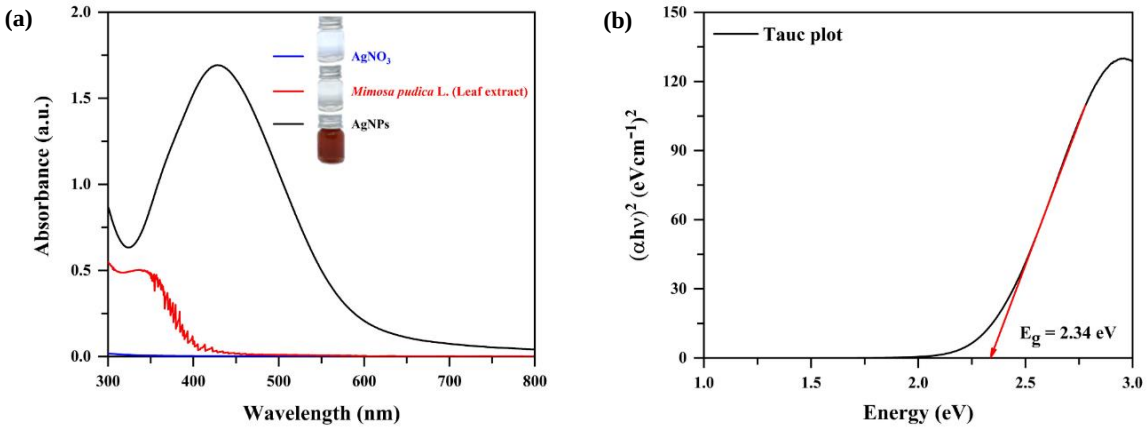

Figure 5 UV-Vis spectra of $AgNO_3$, the extract of *Mimosa pudica* L., and AgNPs (a), and DRS analysis of AgNPs (b)

3.2.2 XRD analysis

Figure 6(a) shows the XRD analysis of AgNPs derived from *Mimosa pudica* L. leaf extract. The characteristic peaks of the diffraction pattern correspond to 2θ values of 28.03°, 32.34°, 38.36°, 44.66°, 46.24°, 54.94°, 57.36°, 64.80° and 77.25°. Peaks at 38.36°, 44.66°, 64.80° and 77.25° correspond to the (111), (200), (220) and (311) crystal planes of face-centered cubic (FCC) metallic silver (JCPDS card No. 04-0783). A second series had additional peaks at 28.03°, 32.34°, 46.24° and 54.94° that are indexed to the (210), (122), (231) and (142) planes of Ag_2O_3 [49]. Mixed Ag/Ag_2O_3 phase formation due to synthesis conditions is induced under high partial oxygen pressure at temperatures >400 °C [49]. As in [50], reactive oxygen species and biomolecules can cause partial oxidation of Ag to Ag_2O_3 in green synthesis, leading to better photocatalytic activity by improved electron-hole pair formation at the metal oxide interface [49, 51]. This synergistic effect benefits methylene blue degradation, as metallic Ag acts as an electron trap, and Ag_2O_3 produces electron-hole pairs under visible light, thus reducing the recombination rate [52, 53].

3.2.3 FTIR analysis

FTIR analysis was employed to identify the functional groups responsible for AgNP reduction and stabilization. FTIR spectra of *Mimosa pudica* L. leaf powder show characteristic bands at 3289, 2917, 2852, 1731, 1606, and 1437 cm^{-1} in Figure 6(b). C-H stretching vibrations in aromatic structures are represented by bands at 2917 and 2852 cm^{-1}. O-H stretching vibrations of phenolic compounds give rise to the broad band at 3289 cm^{-1}. C=C stretching of aromatic rings presents peaks at 1731 and 1606 cm^{-1}, C-O stretching of polyphenols shows a peak at 1437 cm^{-1} [54, 55]. Peak shifts from 3289 cm^{-1} to 3340 cm^{-1} and 1606 cm^{-1} to 1634 cm^{-1} occur after AgNPs have formed, indicating the participation of hydroxyl and phenolic groups in the reduction and stabilization of Ag^+. Both reducing and capping agents of biomolecules from *Mimosa pudica* L. extract were previously reported [56]. Such capabilities arise from the high phytochemical content of alkaloids, polyphenols, tannins and flavonoids in extracts [44]. These hydroxyl groups donate electrons for Ag^+ to Ag^0 reduction, and their aromatic nature provides surface adsorption stabilization [57, 58].

3.2.4 EDX analysis

Elemental composition and purity of the synthesized AgNPs were determined using EDX spectroscopy. The EDX spectrum (Figure 6(c)), shows peaks of silver (Ag), oxygen (O), carbon (C), silicon (Si), sulfur (S) and copper (Cu). Successful formation of AgNPs is confirmed by prominent Ag peaks [59]. Silver oxide phases found in XRD analysis are supported by oxygen signals. Plant-extract organic compounds in the form of capping and stabilizing agents are represented by carbon and oxygen peaks [60]. Sulfur-containing biomolecules from *Mimosa pudica* L. stabilized AgNPs form via sulfur-silver interactions. The sample preparation grid [61] emits copper signals, while silicon is a trace element in the plant extract [62].

3.2.5 TEM analysis

The morphology and size distribution of AgNPs were investigated using transmission electron microscopy (TEM). TEM micrographs of partially spherical particles show monodispersity (Figure 7(a)). Their crystal nature was confirmed using high-resolution lattice fringes with an interplanar spacing (d) of 0.27 nm, which matched that of the (111) plane of the face-centered cubic (FCC) silver structure in Figure 7(b) [63, 64]. Their average diameter was 7.39±2.37 nm determined using ImageJ analysis (Figure 7c). *Mimosa pudica* L. extract controlled particle growth by the action of capping biomolecules [65]. Increased surface area for catalytic reactions, small size, and uniform distribution were provided [66]. Plant extract with optimized synthesis typically yields spherical morphology and small particle sizes. Phytochemicals can shape and control particle size demonstrating their capability to modulate nucleation and growth [67, 68].

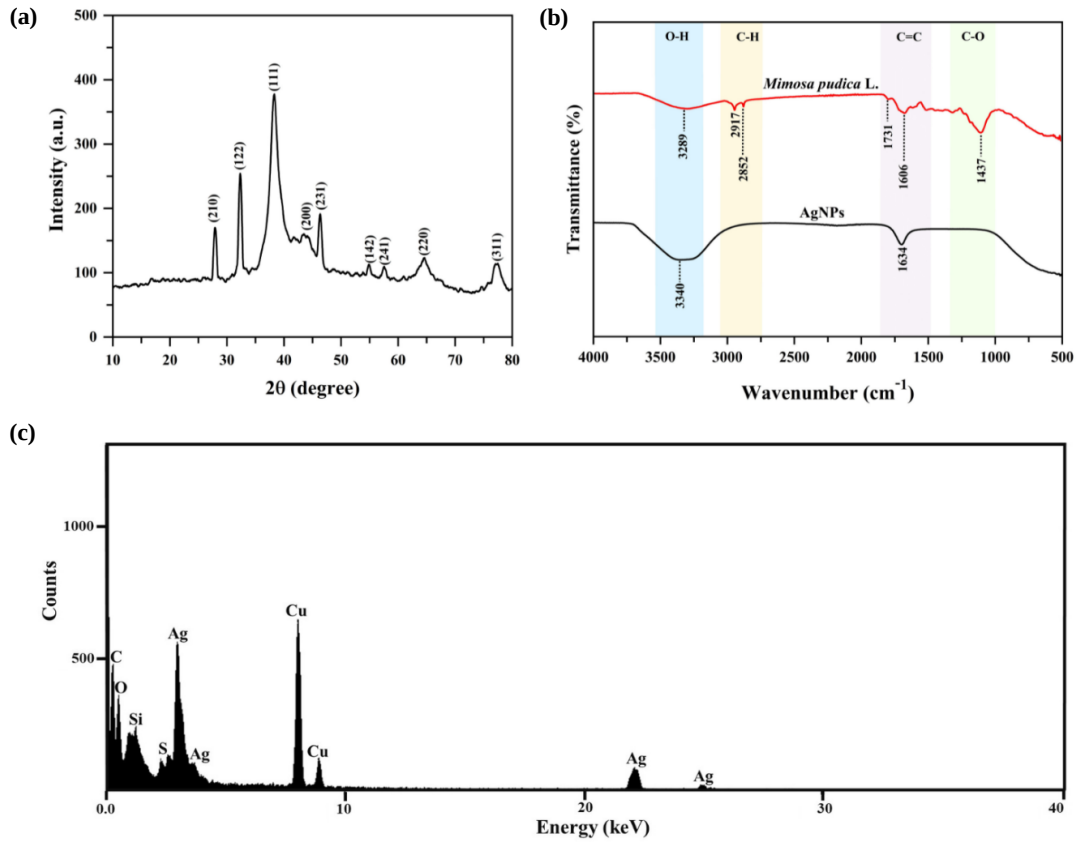

Figure 6 XRD of AgNPs (a), FTIR spectra of AgNPs and *Mimosa pudica* L. leaf powder (b), and EDX of AgNPs (c)

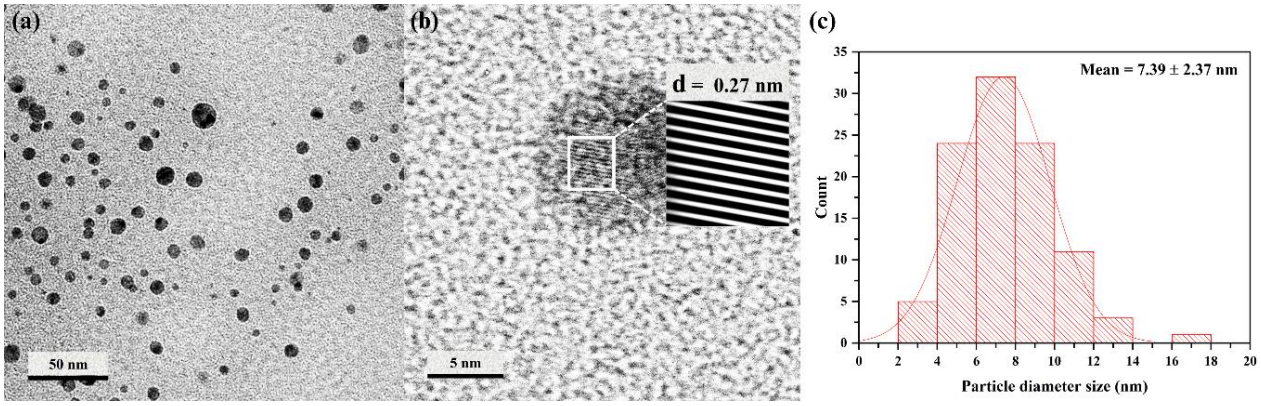

Figure 7 TEM imagery analyzed at 20 nm (a), and 5 nm (b), particle diameter distribution histogram of AgNPs (c)

3.3 Photocatalytic decolorization of MB dye

3.3.1 Optimization for photocatalytic degradation of MB dye

Table 4 shows experimental results from 20 runs executed under different conditions. ANOVA was performed to identify interactions of the factors and the individual factor significance. Equation (5) predicts MB degradation, while Table 6 shows ANOVA results that indicate the influence of quadratic terms on experimental responses. The primary influential parameters were C (reaction time), A (dye concentration), and B (catalyst volume), in descending order. The positive signs of C and B indicate increased MB degradation. Parameter A is negative, so MB degradation decreases with increasing A [29, 38].

$$Y = 65.33 - 5.01A + 2.67B + 7.48C - 1.44AB + 2.35AC - 3.35BC - 0.3606A^2 + 1.96B^2 - 1.15C^2 \quad (5)$$

The predicted response is denoted as *Y*. A, B, and C represent dye concentration, catalyst volume, and reaction time, respectively. Individual variables expressed antagonistic or synergistic effects indicated by their respective negative and positive symbols [29, 69]. The p-values in Table 6 indicate the impact of model terms on MB degradation as follows: C > A > B > BC > B^2 > AC > C^2 > AB > A^2. These results yield a high F-value (25.20) and a low p-value (<0.0001) for the model. Some model parameters (A, B, C, AC, BC, and B^2) are statistically significant [26, 27, 29]. The p-values of model terms AB, A^2, and C^2 are greater than 0.05, and therefore are not statistically significant. Additionally, the lack-of-fit can be used to show model significance. The selected regression model was significant, as shown by the non-significant lack-of-fit, p=0.0572 and F=4.71. Furthermore, model accuracy was confirmed with a low

coefficient of variation (C.V.), 3.84%. According to these results, a signal-to-noise ratio of 17.0208 is acceptable [29]. The fit of the model was also verified using the coefficient of determination (R^2). The predicted R^2 (0.7221) and adjusted R^2 (0.9198) values of the models are statistically significant. Figure 8(a) shows a positive correlation (R^2=0.9578) between the parameters and response (MB degradation, %) according to Equation (5). Figure 8(a) presents an RSM model-generated depiction of the experimental and predicted values of the MB degradation. The percentage of MB degradation shows a satisfactory fit [29].

Table 6 ANOVA for photocatalytic degradation of MB dye

Source	SS	df	MS	F-Value	p-Value	Remark
Model	1438.47	9	159.83	25.20	<0.0001	significant
A	342.74	1	342.74	54.03	<0.0001	
B	97.46	1	97.46	15.36	0.0029	
C	763.13	1	763.13	120.31	<0.0001	
AB	16.63	1	16.63	2.62	0.1365	
AC	44.21	1	44.21	6.97	0.0247	
BC	89.62	1	89.62	14.13	0.0037	
A^2	1.87	1	1.87	0.2955	0.5986	
B^2	55.56	1	55.56	8.76	0.0143	
C^2	19.09	1	19.09	3.01	0.1134	
Residual	63.43	10	6.34			
Lack of Fit	52.32	5	10.46	4.71	0.0572	not significant
Pure Error	11.12	5	2.22			
Cor Total	1501.90	19				

SS: sum of squares; df: degrees of freedom; MS: mean square; F: frequency; p: probability; R^2=0.9578; Pred. R^2=0.7221; Adj. R^2=0.9198; Adequate Precision=17.0208; C.V.=3.84%.

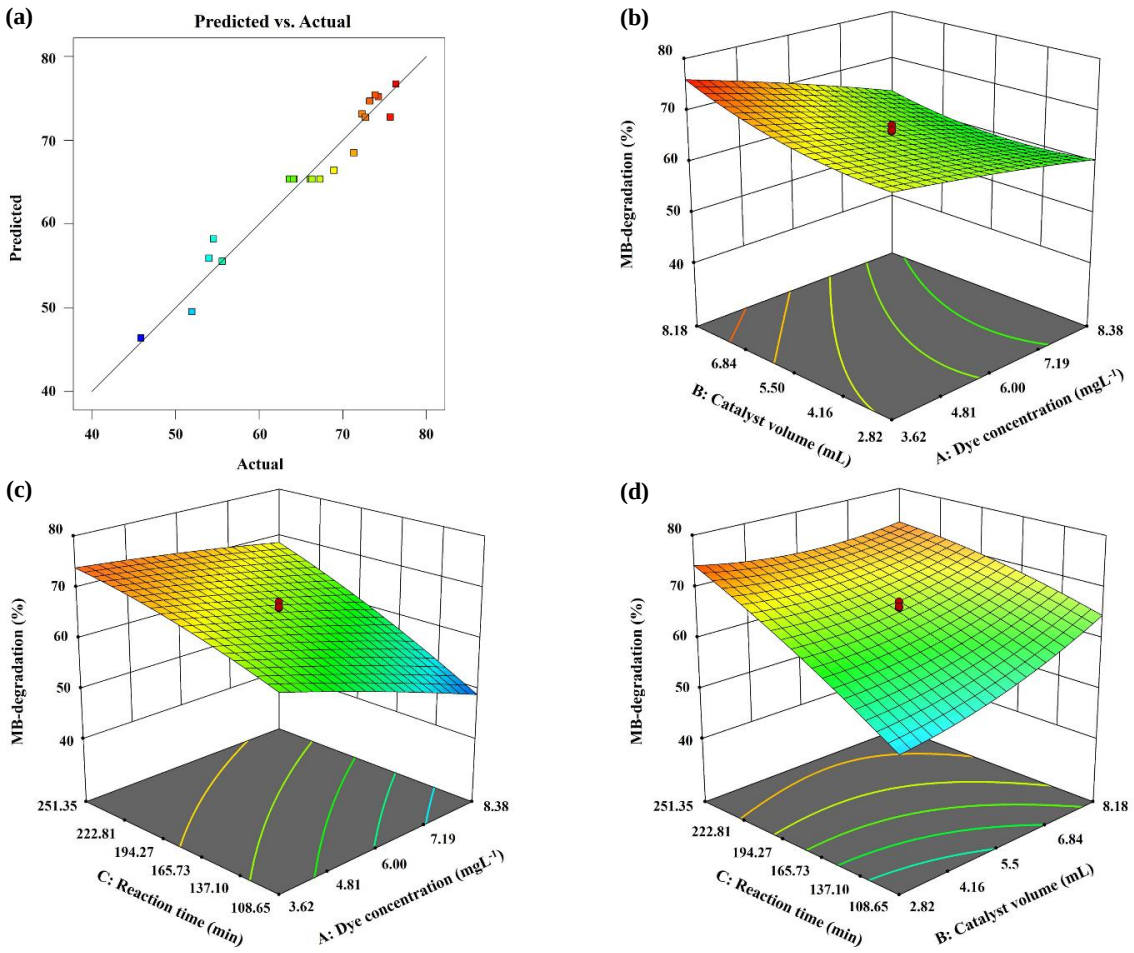

Figure 8 Predicted vs. actual data for degradation efficiency of MB dye (a), 3D plots of interaction between dye concentration and catalyst volume (b), 3D plots of interaction between dye concentration and reaction time (c), and 3D plots of interaction between catalyst volume and reaction time (d) for the photocatalytic degradation of MB dye

3.3.2 Influences of factors and their interaction on MB dye degradation

As illustrated in Figure 8(b), the degradation of MB dye in an aqueous solution is affected by the concentration of dye and the volume of catalyst. With a greater AgNP catalyst volume, MB degradation increases owing to solar light penetration, along with an increased number of active sites on AgNP surfaces. Increasing the photocatalyst volume of AgNPs to absorb more photons results in a greater number of active radicals (oxygen and hydroxyl radicals), resulting in higher degradation. At greater dye concentrations,

photocatalytic degradation declines and more dye molecules reside on catalyst surfaces. Active sites become occupied, resulting in less hydroxyl radical generation, shortening the mean free path of light in the solution [27].

The effect of dye concentration and reaction time on MB degradation is shown in Figure 8(c). AgNPs are excited from the 4d to the 5sp orbital upon UV irradiation from sunlight, resulting in photogenerated electrons for oxidation of MB. These electrons transform oxygen molecules and hydroxyl ions into superoxide radical anions and hydroxyl radicals, respectively. The radicals oxidize MB dye and, in turn, create holes in the d-orbital of AgNPs. These generated holes subsequently decay MB further by capturing electrons from MB dye molecules adsorbed on the AgNP surfaces [70]. The surface of the AgNP photocatalyst is exposed longer to the solar light as the process continues. An increased number of hydroxyl radicals are produced that degrade a greater amount of MB [71]. When the dye concentration is high, the efficiency of MB dye degradation decreases, likely due to insufficient active sites. More dye molecules adsorbed on the catalyst surface with dye in higher concentrations necessitate more reactive species for degradation. Superoxide radical anions and hydroxyl radical production on the catalyst surface are constant with a set catalyst dose and reaction time. Consequently, there are insufficient hydroxyl radicals to break down dye at higher concentrations. Absorption of photons by MB dye also diminishes the generation of hydroxyl radicals on the catalyst surface. Increased dye degradation is related to greater irradiation intensity. At lower dye concentrations, light penetration at greater depth allows degradation at longer distances from the light source. At higher concentrations, degradation slows at longer distances from the light source due to reduced light penetration [27].

The effect of reaction time and catalyst volume on MB dye degradation is shown in Figure 8(d). Degradation efficiency increases as reactors operate for extended periods and with higher catalyst volumes. An increase in these parameters improves the degradation efficiency [27]. With longer treatment times, more of the AgNP photocatalyst surface is exposed to solar light, therefore creating more hydroxyl radicals that can photodegrade larger amounts of MB. As sample loading was increased, photocatalytic activity slowed [71].

The optimal conditions for MB degradation were a catalyst volume of 8.20 mL, reaction time of 231 min, and an MB concentration of 3.64 mgL^{-1}. Experimental and predicted values for MB degradation were 79.07 and 76.66%, respectively. Moreover, the model predictions for photocatalytic degradation of MB dye were further validated by comparison with experimental values. The synthesized AgNPs could better photodegrade MB dye [72] compared to other systems reported in the literature (Table 7).

Table 7 Comparison of the photocatalytic activity of synthesized AgNPs and catalysts from the literature

Catalyst	Dyes	Variables	Time (min)	Degradation (%)	References
AgNPs	OG	Dosage: 0.05 g Volume: 100 mL Dye: 15 mgL^{-1}	180	70.61%	[73]
AgNPs	CV, CBB	Dosage: 50 mg Volume: 100 mL Dye : N/A	180	87.00% 74.00%	[74]
AgNPs	CR, CB, CV	Dosage: 10 mg Volume: N/A Dye: N/A	1,440	>95.00% 90.00% >90.00%	[75]
AgNPs	MB	Dosage: 10 mg Volume: 200 mL Dye: 1mg/100 mL	150	98.84%	[76]
AgNPs	MB	Dose: 8.2 mL Volume: 30 mL Dye: 3.64 mgL^{-1}	231	79.07%	This study

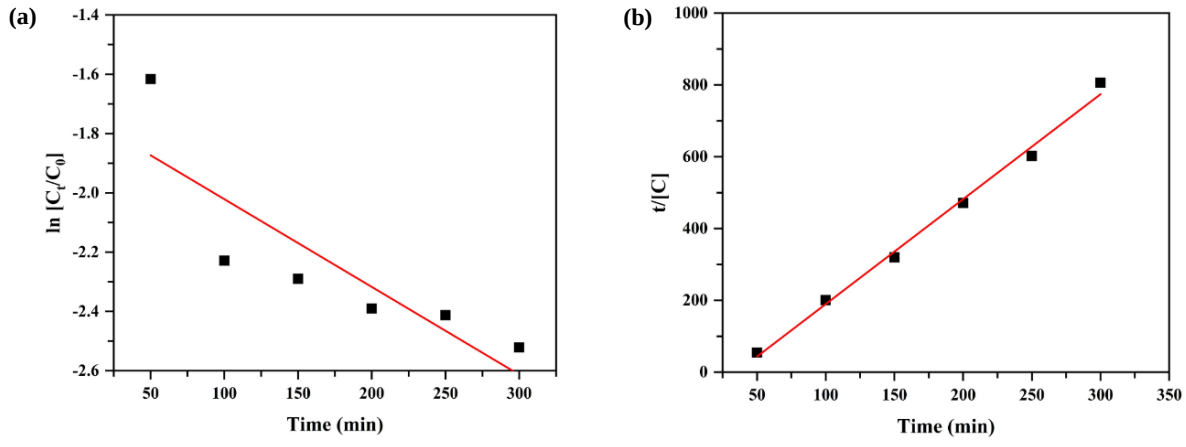

Figure 9 Kinetic plots of pseudo-first-order (a), and pseudo-second-order (b) models

3.3.3 Kinetics study

Investigation of kinetics involved pseudo-first-order and pseudo-second-order models, as depicted in Figure 9 [77, 78]. Data were fit well using the pseudo-second-order kinetic model, indicated by its higher regression coefficient (R^2=0.9990) opposed to a pseudo-first-order kinetic model (R^2=0.7323). Additionally, the rate constant (k) estimated for the pseudo-second-order model is 0.0929 mg^{-1} L min^{-1}. [77] reported that a pseudo-second-order kinetic model implies that the adsorption process is governed by chemical reactions and not physical processes. The k and R^2 values of the pseudo-first and pseudo-second-order models are shown in Table 8.

Table 8 Data on the kinetic models of photocatalytic degradation of MB dye

Model	Equation	Rate constant, k	R^2 values
Pseudo-first-order	$\ln(C/C_0) = -k_1 t$	0.0030 min^{-1}	0.7323
Pseudo-second-order	$\frac{t}{C} = \frac{t}{C_0} - \frac{1}{k_2 C_0^2}$	0.0929 mg^{-1} L min^{-1}	0.9990

C_0 represents the initial concentration of the dye, while C denotes the final concentration. The parameters t, k_1, and k_2 represent time, the rate constant of pseudo-first-order, and the rate constant of pseudo-second-order models, respectively.

3.3.4 Proposed mechanism of photocatalytic degradation of MB dye

Synthesized AgNPs were used for methylene blue (MB) degradation under solar light irradiation. The semiconductor behavior of green-synthesized AgNPs using *Mimosa pudica* L. leaf extract as a stabilizing agent was shown with a 2.34 eV band gap derived from a Tauc plot (Figure (5b)). This bandgap predicts photocatalysis by direct light-to-energy conversion of solutes through semiconductor charge carriers, potentially for photooxidation-based organic water pollutant removal [79]. Solar light-irradiated AgNPs function as nanocatalysts for MB photocatalytic degradation (Figure 10). Their (positive holes, h^+, and conduction electrons, e^-) are generated by electrons excited from the valence band (VB) to the conduction band (CB) at or above the energy required for solar excitation (bandgap energy) [80, 81]. MB is broken down by these CB electrons, which react with oxygen to form superoxide radical anions, and by VB holes, which react with water molecules to produce hydroxyl radicals [15].

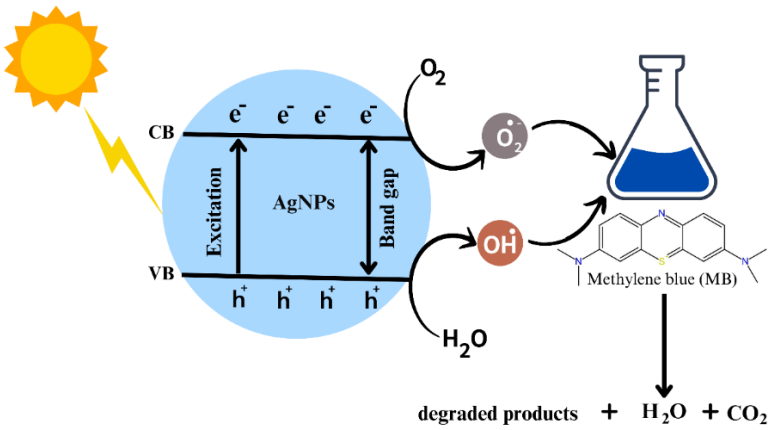

Figure 10 Proposed mechanism of photocatalytic degradation of MB dye

4. Conclusions

Mimosa pudica L. leaf extract was used for green synthesis of AgNPs and successfully optimized. Applying RSM based on CCD is useful for modeling and optimizing AgNP synthesis. Analysis of variance of the regression model suggests that the model well fitted the experimental data, which was supported by a strong correlation coefficient (R^2=0.9873). The presence of polyphenols and flavonoids in *Mimosa pudica* L. leaf extract was confirmed with FTIR analysis. They served as effective capping and reducing agents in the synthesis process. AgNPs were demonstrated as nanoparticles with uniform spherical morphology and an average diameter of 7.39±2.37 nm in a TEM investigation. Elemental composition of the AgNPs was done by EDX analysis showing a significant peak for silver absorption, verifying successful AgNP synthesis. XRD analysis confirmed the FCC crystalline structure of AgNPs, which improved photocatalytic activity. The photodegradation of methylene blue dye was done by the synthesized AgNPs under solar light irradiation, which was successfully optimized using RSM based on CCD. The high correlation coefficient (R^2=0.9578) indicated an excellent fit of the regression model to the experimental data. A very high percentage of degradation, 79.07%, was achieved under optimal conditions. From kinetic studies, the degradation followed pseudo-second-order kinetics, revealing that the process was dependent upon chemical reactions, not physical adsorption. A successful application of green synthesis combined with statistical optimization techniques for production of photocatalytically active AgNPs for use in environmental remediation is demonstrated in this study.

5. Acknowledgements

Chaison P, Wittayanarakul K, and Sriuttha M express their gratitude to Research and Graduate Studies (RP64-4-002) at Khon Kaen University for providing financial support.

6. References

[1] Mosavi SA, Ghadi A, Gharbani P, Mehrizad A. Photocatalytic removal of methylene blue using Ag@CdSe/Zeoilte nanocomposite under visible light irradiation by response surface methodology. Mater Chem Phys. 2021;267:124696.
[2] Gharbani P, Mehrized A, Jafarpour I. Adsorption of penicillin by decaffeinated tea waste. Pol J Chem Technol. 2015;17(3):95-9.
[3] Mehrizad A, Gharbani P. Optimization of operational variables and kinetic modeling for photocatalytic removal of direct blue 14 from aqueous media by ZnS nanoparticles. J Water Health. 2017;15(6):955-65.

[4] Mehrizad A, Gharbani P. Synthesis of ZnS decorated carbon fibers nanocomposite and its application in photocatalytic removal of rhodamine 6G from aqueous solutions. Prog Color Colorants Coat. 2017;10:13-21.
[5] Couto SR. Dye removal by immobilised fungi. Biotechnol Adv. 2009;27(3):227-35.
[6] Jasri K, Abdulhameed AS, Jawad AH, ALOthman ZA, Yousef TA, Al Duaij OK. Mesoporous activated carbon produced from mixed wastes of oil palm frond and palm kernel shell using microwave radiation-assisted K_2CO_3 activation for methylene blue dye removal: optimization by response surface methodology. Diam Relat Mater. 2023;131:109581.
[7] Dbik A, El Messaoudi N, Bentahar S, El Khomri M, Lacherai A, Faska N. Optimization of methylene blue adsorption on agricultural solid waste using Box-Behnken Design (BBD) mombined with Response Surface Methodology (RSM) modeling. Biointerface Res Appl Chem. 2022;12(4):4567-83.
[8] Hassanzadeh P, Gharbani P, Derakshanfard F, Maher BM. Preparation and characterization of PVDF/g-C3N4/chitosan nanocomposite membrane for the removal of direct blue 14 dye. J Polym Environ. 2021;29:3693-702.
[9] Quynh HG, Thanh HV, Phuong NTT, Duy NPT, Hung LH, Dung NV, et al. Rapid removal of methylene blue by a heterogeneous photo-Fenton process using economical and simple-synthesized magnetite-zeolite composite. Environ Technol Innov. 2023;31: 103155.
[10] Haider S, Khan SU, Najeeb J, Naeem S, Rafique H, Munir H, et al. Synthesis of cadmium oxide nanostructures by using *Dalbergia sissoo* for response surface methodology based photocatalytic degradation of methylene blue. J Clean Prod. 2022;365:132822.
[11] Qarajehdaghi M, Mehrizad A, Gharbani P, Shahverdizadeh GH. Quaternary composite of CdS/g-C3N4/rGO/CMC as a susceptible visible-light photocatalyst for effective abatement of ciprofloxacin: optimization and modeling of the process by RSM and ANN. Process Saf Environ Prot. 2023;169:352-62.
[12] Moond M, Singh S, Sangwan S, Devi P, Beniwal A, Rani J, et al. Biosynthesis of silver nanoparticles utilizing leaf extract of *Trigonella foenum-graecum* L. for catalytic dyes degradation and colorimetric sensing of Fe^{3+}/Hg^{2+}. Molecules. 2023;28(3):951.
[13] Rasheed A, Hussain S, Mushtaq W, Zubair M, Siddique K, Attia K, et al. Application of silver nanoparticles synthesized through varying biogenic and chemical methods for wastewater treatment and health aspects. Environ Sci Pollut Res. 2023:1-17.
[14] Albeladi SSR, Malik MA, Al-thabaiti SA. Facile biofabrication of silver nanoparticles using *Salvia officinalis* leaf extract and its catalytic activity towards congo red dye degradation. J Mater Res Technol. 2020;9(5):10031-44.
[15] Alshehri AA, Malik MA. Phytomediated photo-induced green synthesis of silver nanoparticles using *Matricaria chamomilla* L. and its catalytic activity against rhodamine B. Biomolecules. 2020;10(12):1604.
[16] Dua TK, Giri S, Nandi G, Sahu R, Shaw TK, Paul P. Green synthesis of silver nanoparticles using *Eupatorium adenophorum* leaf extract: characterizations, antioxidant, antibacterial and photocatalytic activities. Chem Pap. 2023;77:2947-56.
[17] Rajasekar R, Thanasamy R, Samuel M, Edison TNJI, Raman N. Ecofriendly synthesis of silver nanoparticles using *Heterotheca subaxillaris* flower and its catalytic performance on reduction of methyl orange. Biochem Eng J. 2022;187:108447.
[18] Malik MA, Batterjee MG, Kamli MR, Alzahrani KA, Danish EY, Nabi A. Polyphenol-capped biogenic synthesis of noble metallic silver nanoparticles for antifungal activity against *Candida auris*. J Fungi. 2022;8(6):639.
[19] Panyadee P. A review on the ethnobotany of exotic species in Thailand I: *Mimosa pudica* L. (Leguminosae). Thai J Bot. 2022;14(2):79-94.
[20] Muhammad G, Hussian MA, Jantan I, Bukhari SNA. *Mimosa pudica* L., a high-value medicinal plant as a source of bioactives for pharmaceuticals. Compr Rev Food Sci Food Saf. 2016;15(2):303-15.
[21] Baharuddin NS, Roslan MAM, Bawzer MAM, Azzeme AM, Rahman ZA, Khayat ME, et al. Response surface optimization of extraction conditions and in vitro antioxidant and antidiabetic evaluation of an under-valued medicinal weed, *Mimosa pudica*. Plants. 2021;10(8):1692.
[22] Durgadevi G, Karthika N. Screening of phytochemicals and pharmacological studies on *Mimossa pudica* L. Asian J Innov Res. 2018;3(2):19-28.
[23] Hai ND, Dat NM, Huong LM, Tai LT, Thinh DB, Nam NTH, et al. Phytosynthesis of silver nanoparticles using *Mangifera indica* leaves extract at room temperature: Formation mechanism, catalytic reduction, colorimetric sensing, and antimicrobial activity. Colloids Surf B Biointerfaces. 2022;220:112974.
[24] Cardoso-Avila PE, Patakfalvi R, Rodríguez-Pedroza C, Aparicio-Fernández X, Loza-Cornejo S, Villa-Cruz V, et al. One-pot green synthesis of gold and silver nanoparticles using *Rosa canina* L. extract. RSC Adv. 2021;11(24):14624-31.
[25] Kumari SC, Selvakumar V, Padma PN, Anuradha K. Optimization studies on green synthesis of silver nanoparticles from different plant extracts using Taguchi Design. Indian J Sci Technol. 2021;14(38):2888-98.
[26] Ashraf N, Ahmad F, Jie CJ, Di ZT, Feng-Zhu Z, Yin DC. Optimization of *Enterobacter cloacae* mediated synthesis of extracellular silver nanoparticles by response surface methodology and their characterization. Particul Sci Technol. 2020;38(8):931-43.
[27] Ekka B, Sahu MK, Patel RK, Dash P. Titania coated silica nanocomposite prepared via encapsulation method for the degradation of safranin-O dye from aqueous solution: optimization using statistical design. Water Resour Ind. 2019;22:100071.
[28] Gharbani P. Preparation, characterization and application of synthesized nano $Zn(OH)_8Cl_2H_2O$ in removing of dye pollutants: modeling of removal process by response surface methodology. J Mol Liq. 2017;246:317-24.
[29] Rana AG, Minceva M. Analysis of photocatalytic degradation of phenol with exfoliated graphitic carbon nitride and light-emitting diodes using response surface methodology. Catalyst. 2021;11(8):898.
[30] Murshed MK, Dursun AY, Dursun G. Application of response surface methodology on photocatalytic degradation of Astrazon Orange G dye by ZnO photocatalyst: Internal mass transfer effects. Chem Eng Res Des. 2022;188:27-38.
[31] Rasheed T, Bilal M, Li C, Nabeel F, Khalid M, Iqbal HMN. Catalytic potential of bio-synthesized silver nanoparticles using *Convolvulus arvensis* extract for the degradation of environmental pollutants. J Photochem Photobiol B. 2018;181:44-52.
[32] Favier L, Simion AI, Hlihor RM, Fekete-Kertész I, Molnár M, Harja M, et al. Intensification of the photodegradation efficiency of an emergent water pollutant through process conditions optimization by means of response surface methodology. J Environ Manage. 2023;328:116928.
[33] Saratale RG, Cho SK, Saratale GD, Kadam AA, Ghodake GS, Magotra VK, et al. Lignin-mediated silver nanoparticle synthesis for photocatalytic degradation of reactive yellow 4G and in vitro assessment of antioxidant, antidiabetic, and antibacterial activities. Polymers. 2022;14(3):648.

[34] Mehwish HM, Rajoka MSR, Xiong Y, Cai H, Aadil RM, Mahmood Q, et al. Green synthesis of a silver nanoparticle using *Moringa oleifera* seed and its applications for antimicrobial and sun-light mediated photocatalytic water detoxification. J Environ Chem Eng. 2021;9(4):105290.
[35] Awad MA, Hendi AA, Ortashi KM, Alzahrani B, Soliman D, Alanazi A, et al. Biogenic synthesis of silver nanoparticles using *Trigonella foenum-graecum* seed extract: characterization, photocatalytic and antibacterial activities. Sens Actuators A: Phys. 2021;323:112670.
[36] Yerli-Soylu N, Akturk A, Kabak Ö, Erol-Taygun M, Karbancioglu-Guler F, Küçükbayrak S. TiO_2 nanocomposite ceramics doped with silver nanoparticles for the photocatalytic degradation of methylene blue and antibacterial activity against *Escherichia coli*. Eng Sci Technol Int J. 2022;35:101175.
[37] Dinari A, Mamoudi J. Response surface methodology analysis of the photodegradation of methyl orange dye using synthesized TiO_2/Bentonite/ZnO composites. Adv Environ Technol. 2022;8(1):31-46.
[38] Rashbari Y, Abazari M, Arfaeinia L, Gholizadeh A, Afshin S, Poureshgh Y, et al. The optimization of reactive black 5 dye removal in the sono-catalytic process combined with local yellow montmorillonite and hydrogen peroxide using response surface methodology from aqueous solutions. Biomass Conv Bioref. 2023;13:6067-81.
[39] Tosun NG, Kaplan Ö. Optimization of the green synthesis of silver nanoparticle with box-behnken design: using aloe vera plant extract as a reduction agent. Sakarya Univ J Sci. 2021;25(3):774-87.
[40] Dada AO, Inyinbor AA, Idu EI, Bello OM, Oluyori AP, Adelani-Akande TA, et al. Effect of operational parameters, characterization and antibacterial studies of green synthesis of silver nanoparticles using *Tithonia diversifolia*. PeerJ. 2018;6:e5865.
[41] Albadran FH, Kamal IM. Synthesis of green silver nanoparticles by one pot microwave-assisted technique: modeling and optimization. Period Eng Nat Sci. 2020;8(3):1591-9.
[42] Balavandy SK, Shameli K, Biak DRBA, Abidin ZZ. Stirring time effect of silver nanoparticles prepared in glutathione mediated by green method. Chem Cent J. 2014;8:11.
[43] Moosaei R, Sabbaghi S, Zadegan MSJ, Rasouli K, Ghaedi S, Rajabi H. Silver nanoparticles modified titanium carbide MXene composite for RSM-CCD optimised chloride removal from water. J Mol Liq. 2024;399:124480.
[44] Hayatou MU, Tembe EA, Herve B, Borgia NN, Fokunang CN. Qualitative and quantitative phytochemical characterization of leaf extracts of *Mimosa pudica* (Mimosaceae). J Complement Altern Med Res. 2023;23(2):1-13.
[45] Karan T, Gonulalan Z, Erenler R, Kolemen U, Eminagaoglu O. Green synthesis of silver nanoparticles using *Sambucus ebulus* leaves extract: Characterization, quantitative analysis of bioactive molecules, antioxidant and antibacterial activities. J Mol Struct. 2024;1296:136836.
[46] Gomathi M, Rajkumar PV, Prakasam A, Ravichandran K. Green synthesis of silver nanoparticles using *Datura stramonium* leaf extract and assessment of their antibacterial activity. Resource-Efficient Technologies. 2017;3(3):280-4.
[47] Saied E, Hashem AH, Ali OM, Selim S, Almuhayawi MS, Elbahnasawy MA. Photocatalytic and antimicrobial activities of biosynthesized silver nanoparticles using *Cytobacillus firmus*. Life. 2022;12(9):1331.
[48] Shah MZ, Guan ZH, Din AU, Ali A, Rehman AU, Jan K, et al. Synthesis of silver nanoparticles using *Plantago lanceolata* extract and assessing their antibacterial and antioxidant activities. Sci Rep. 2021;11:20754.
[49] Semaltianos NG, Perries W, Romani S, Potter RJ, Dearden G, Watkins KG. Polymer-nanoparticle composites composed of PEDOT:PSS and nanoparticles of Ag synthesised by laser ablation. Colloid Polym Sci. 2012;290(3):213-20.
[50] Korkmaz N, Karadag A. Microwave assisted green synthesis of Ag, Ag_2O, and Ag_2O_3 Nanoparticles. JOTCSA. 2021;8(2):585-92.
[51] Meng Y. A sustainable approach to fabricating Ag nanoparticles/PVA hybrid nanofiber and its catalytic activity. Nanomaterials. 2015;5(2):1124-35.
[52] Danish MSS, Estrella-Pajulas LL, Alemaida IM, Grilli ML, Mikhylov A, Senjyu T. Green synthesis of silver oxide nanoparticles for photocatalytic environmental remediation and biomedical applications. Metals. 2022;12(5):769.
[53] Ziashahabi A, Prato M, Dang Z, Poursalehi R, Naseri N. The effect of silver oxidation on the photocatalytic activity of Ag/ZnO hybrid plasmonic/metal-oxide nanostructures under visible light and in the dark. Sci Rep. 2019;9(1):11839.
[54] Ahuchaogu AA, Ogbuehi GI, Ukaogo PO, Otuokere IE. Gas chromatography mass spectrometry and fourier transform infrared spectroscopy analysis of methanolic extract of *Mimosa pudica* L. leaves. J Drugs Pharm Sci. 2020;4(1):1-9.
[55] Dhanush C, Aravindh S, Jesreena JS, Nagadharshini R, Jano N, Almeer R, et al. Biomimetic synthesis of carbon dots from *Mimosa pudica* leaves for enhanced bioimaging. Waste Biomass Valor. 2025;16(2):713-21.
[56] Sreenivasulu V, Kumar NS, Suguna M, Asif M, Al-Ghurabi EH, Huang ZX, et al. Biosynthesis of silver nanoparticles using *Mimosa Pudica* plant root extract: characterization, antibacterial activity and electrochemical detection of dopamine. Int J Electrochem Sci. 2016;11(12):9959-71.
[57] Velmurugan G, Chohan JS, Suresh Kannan V, Paramasivam P, Siva Shankar V, Maranan R. Green synthesis of silver nanoparticles from southern *Eucalyptus globulus*: potent antioxidants and photocatalysts for rhodamine B dye degradation. Desalin Water Treat. 2024;320:100687.
[58] Shen L, Chen M, Hu L, Chen X, Wang J. Growth and stabilization of silver nanoparticles on carbon dots and sensing application. Langmuir. 2013;29(52):16135-40.
[59] Edison TNJI, Atchudan R, Sethuraman MG, Lee YR. Reductive-degradation of carcinogenic azo dyes using *Anacardium occidentale* testa derived silver nanoparticles. J Photochem Photobiol B. 2016;162:604-10.
[60] Ravichandran V, Vasanthi S, Shalini S, Shah SAA, Harish R. Green synthesis of silver nanoparticles using *Atrocarpus altilis* leaf extract and the study of their antimicrobial and antioxidant activity. Mater Lett. 2016;180:264-7.
[61] Shankar PD, Shobana S, Karuppusamy I, Pugazhendhi A, Ramkumar VS, Arvindnarayan S, et al. A review on the biosynthesis of metallic nanoparticles (gold and silver) using bio-components of microalgae: formation mechanism and applications. Enzyme Microb Technol. 2016;95:28-44.
[62] Yassin MT, Mostafa AAF, Al-Askar AA, Al-Otibi FO. Facile green synthesis of silver nanoparticles using aqueous leaf extract of *Origanum majorana* with potential bioactivity against multidrug resistant bacterial strains. Crystals. 2022;12(5):603.
[63] Shruthi G, Prasad KS, Vinod TP, Balamurugan V, Shivamallu C. Green synthesis of biologically active silver nanoparticles through a phyto-mediated approach using *Areca catechu* leaf extract. ChemistrySelect. 2017;2(32):10354-9.

[64] Fan Y, Liu Z, Wang L, Zhan J. Synthesis of starch-stabilized Ag nanoparticles and Hg recognition in aqueous media. Nanoscale Res Lett. 2009;4(10):1230.
[65] Fatimah I, Mutiara NAL. Biosynthesis of silver nanoparticles using Putri Malu (*Mimosa pudica*) leaves extract and microwave irradiation method. Molekul. 2016;11(2):288-98.
[66] Prabula SS, Hentry C, Al-Farraj S, Kumar PR, Sillanpää M, Aravind M. Activity of *Bambusa vulgaris* extract in reducing silver nanoparticles: evaluation against methylene blue organic pollutant and microbial agents. Discov Appl Sci. 2024;6(4):142.
[67] Zuhrotun A, Oktaviani DJ, Hasanah AN. Biosynthesis of gold and silver nanoparticles using phytochemical compounds. Molecules. 2023;28(7):3240.
[68] Velgosova O, Dolinská S, Podolská H, Mačák L, Čižmárová E. Impact of plant extract phytochemicals on the synthesis of silver nanoparticles. Materials. 2024;17(10):2252.
[69] Hong G, Wang Y. Synthesis of low-cost adsorbent from rice bran for the removal of reactive dye based on the response surface methodology. Appl Surf Sci. 2017;423:800-9.
[70] Tam KT, Thanh DV, Van HT, Mai NTP, Hai CT, Phoung TM, et al. Green synthesis of silver nanoparticles using extract of *Disporopsis Longifolia* for photocatalytic degradation of methylene blue. Am J Environ Sci. 2022;18(5):116-24.
[71] Siddiqui VU, Ansari A, Ansari MT, Akram MK, Siddiqi WA, Alosaimi AM, et al. Optimization of facile synthesized ZnO/CuO nanophotocatalyst for organic dye degradation by visible light irradiation using response surface methodology. Catalysts. 2021;11(12):1509.
[72] Khane Y, Benouis K, Albukhaty S, Sulaiman GM, Abomughaid MM, Ali AA, et al. Green synthesis of silver nanoparticles using aqueous *Citrus limon* zest extract: characterization and evaluation of their antioxidant and antimicrobial properties. Nanomaterials. 2022;12(12):2013.
[73] Aslam M, Fozia F, Gul A, Amed I, Ullah R, Bari A, et al. Phyto-extract-mediated synthesis of silver nanoparticles using aqueous extract of *Sanvitalia procumbens*, and characterization, optimization and photocatalytic degradation of azo dyes orange G and direct blue-15. Molecules. 2021;26(20):6144.
[74] Seerangaraj V, Sathiyavimal S, Shankar SN, Nandagopal JGT, Balashanmugam P, Al-Misned FA, et al. Cytotoxic effects of silver nanoparticles on *Ruellia tuberosa*: photocatalytic degradation properties against crystal violet and coomassie brilliant blue. J Environ Chem Eng. 2021;9(2):105088.
[75] Nga NTA, Raghavendra VB, Sindhu R, Alshiekheid M, Sabour A, Krishnan R, et al. Green fabrication of silver nanoparticles using *Chloroxylon swietenia* leaves and their application towards dye degradation and food borne pathogens. Food Chem Toxicol. 2022;165:113192.
[76] Khalil S, Mehmood A, Khan MAR, Ahmed KS, Abasi F, Raffi M, et al. Antibacterial, antioxidant and photocatalytic activity of novel *Rubus ellipticus* leaf mediated silver nanoparticles. J Saudi Chem Soc. 2023;27(1):101576.
[77] Nazim M, Khan AAP, Asiri AM, Kim JH. Exploring rapid photocatalytic degradation of organic pollutants with porous CuO nanosheets: synthesis, dye removal, and kinetic studies at room temperature. ACS Omega. 2021;6(4):2601-12.
[78] Agnihotri S, Sillu D, Sharma G, Arya RK. Photocatalytic and antibacterial potential of silver nanoparticles derived from pineapple waste: process optimization and modeling kinetics for dye removal. Appl Nanosci. 2018;8:2077-92.
[79] Wang X, Wang F, Sang Y, Liu H. Full-spectrum solar-light-activated photocatalysts for light–chemical energy conversion. Adv Energy Mater. 2017;7(23):1700473.
[80] Abdel Messih MF, Ahmed MA, Soltan A, Anis SS. Synthesis and characterization of novel Ag/ZnO nanoparticles for photocatalytic degradation of methylene blue under UV and solar irradiation. J Phys Chem Solids. 2019;135:109086.
[81] Alshehri AA, Malik MA. Biogenic fabrication of ZnO nanoparticles using *Trigonella foenum-graecum* (Fenugreek) for proficient photocatalytic degradation of methylene blue under UV irradiation. J Mater Sci: Mater Electron. 2019;30:16156-6173.